Magnetic properties of narrow zig-zag graphene nanoribbons from *ab initio* calculations

A Thesis

submitted to

Indian Institute of Science Education and Research Pune

in partial fulfilment of the requirements for the

BS-MS Dual Degree Programme

By

Raghavendra Meena

Indian Institute of Science Education and Research Pune

Dr. Homi Bhabha Road,

Pashan, Pune 411008, INDIA.
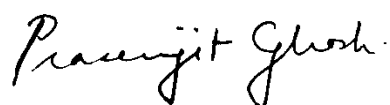
May, 2020

Supervisors: Prof. Michele Casula and Prof. Prasenjit Ghosh,

Certificate

This is to certify that this dissertation entitled "Magnetic properties of narrow zig-zag graphene nanoribbons from *ab initio* calculations" towards the partial fulfilment of the BS-MS dual degree program at the Indian Institute of Science Education and Research, Pune represents study/work carried out by Raghavendra Meena at Sorbonne University, Paris under the supervision of Prof. Michele Casula, CNRS researcher, and HOD, TQM group, IMPMC during the academic year 2019-2020.

Prof. Michele Casula

CNRS Researcher,

Head of TQM, IMPMC,

Sorbonne University,

Paris, France

Prof. Prasenjit Ghosh,

Associate Professor,

CMS Group,

IISER Pune,

Maharashtra, India

TAC:

Supervisor: Prof. Michele Casula

Expert: Prof. Mukul Kabir

This thesis is dedicated to my late uncle Hanuman Meena.

Declaration

I hereby declare that the matter embodied in the report entitled "Magnetic properties of narrow zig-zag graphene nanoribbons from *ab initio* calculations" are the results of the work carried out by me at the TQM group, IMPMC, Sorbonne University, Paris, under the supervision of Prof. Michele Casula and the same has not been submitted elsewhere for any other degree.

Michele Casula

Raghavendra Meena

Acknowledgements

First and foremost, I would like to thank my supervisor Prof. Michele Casula and co-supervisor, Prof. Prasenjit Ghosh, for coming up with this collaborative project. Thank you for introducing me to the field of Computational Materials Science and also for answering my innumerable questions, providing continuing support, giving constructive comments and suggestions, and for opening up many more opportunities for my future. Without you, this work would not have been possible.

I wish to thank the European Union (EU) for coming up with an idea of collaboration between IISER Pune and Sorbonne University within the framework of the Erasmus+ Inter-Institutional credit mobility program. Thank you for supporting me financially as well. I am also grateful to the administration staff of IISER Pune and Pierre and Marie Curie University, France, for the hospitality, smooth processing of the paperwork, and helping me with the accommodation.

I would also like to thank Romain and Tommaso for being there to help me in learning quantum Monte Carlo and TurboRVB package, and for their many helpful comments and suggestions.

I would like to express my gratitude to Niharika, Nisha, Unmesh, Ashwathi, Kanika, Gautam, Vineet, and Hossain, who are part of Prof. Ghosh's group, for helping me in understanding the Density functional theory and QuantumESPRESSO package.

I would like to thank the Faculty and entire community at IISER Pune for their unconditional support throughout my studies. I am especially thankful to my friends for creating all the much-cherished memories at IISER, Pune.

Next, many thanks to the Institute for Development and Scientific Computing resources (IDRIS) for providing access to the HPC machine (Jean-Zay), which helped me in completing my work within time.

Last but not least, I am thankful to my parents for believing in me and sending me thousands of kilometres away from them so that I could do science.

Contents

List of Figures

List of Tables

Abstract

The graphene nanoribbons are one-dimensional strips of graphene, which are intensively studied because of their remarkable electronic and magnetic properties. In this work, we have studied the zig-zag type ribbons, because it has already been proposed that magnetic edges-states, present in the ground state at the Fermi, could be relevant for spintronic applications. In this report, we have tried to give a reliable description of the ground state of the zig-zag ribbons. At the density functional theory (DFT) level, it is believed that the antiferromagnetic phase is the ground state for both molecular and extended systems. However, the DFT results quantitatively depend on the chosen functional. Moreover, quantum Monte Carlo (QMC), a more accurate high-level theory, predicts the paramagnetic phase to be the ground state for the acene series, the molecular analogue of the narrowest zig-zag graphene nanoribbons. Since these systems are strongly correlated, DFT needs to be validated against a benchmark theory, such as QMC. In this report, we carry out extensive variational and diffusion QMC calculations, and we show that in the ribbon the antiferromagnetic phase is energetically more stable than the simple paramagnetic wavefunction. The QMC energy gains and the magnetic moments are comparable to those obtained by the DFT-GauPBE exchange-correlation (XC) functional. It turns out that the energetics of static magnetic configurations at the GauPBE level is more accurate than the one from the PBE XC-functional for such a strongly correlated system.

Chapter 1: Introduction

In the 21st century, arguably graphene is the most studied material in the field of materials science because of its remarkable physical and chemical properties, e.g., graphene is one of the strongest materials ever tested[1]. Apart from these basic properties, researchers are also interested in the optical and electronic properties of graphene. Like graphene, its derivatives also exhibit interesting properties. In this work, we will focus on one of the graphene derivatives, zig-zag graphene nanoribbons.

The graphene nanoribbons are one-dimensional strips of graphene. The graphene nanoribbons are classified into two categories based on their edge structures - armchair or zig-zag - as shown in Figure 1.
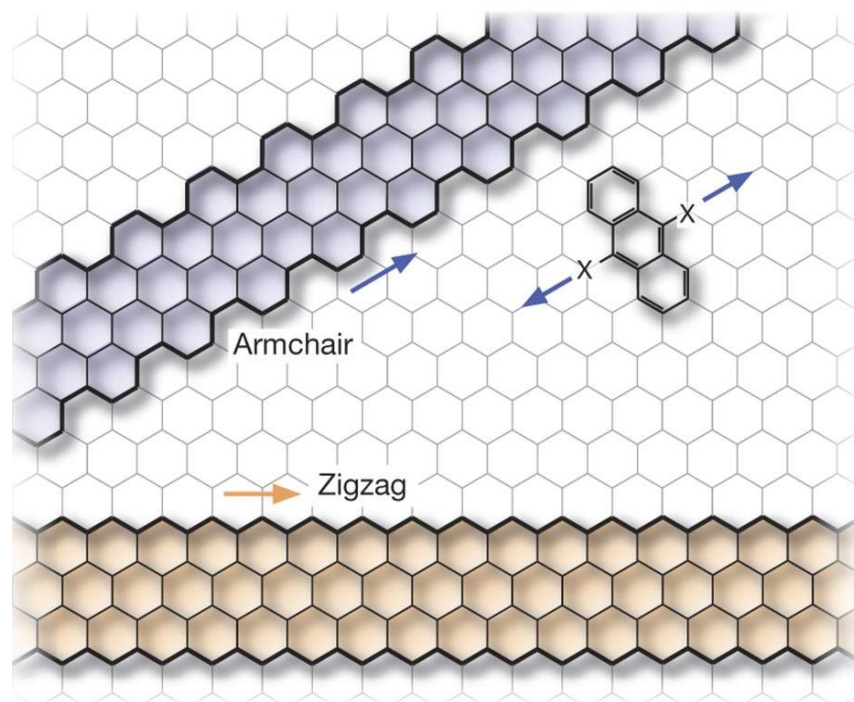
Figure 1: Armchair and Zig-zag graphene nanoribbons. Illustration by Ruffieux et al. Nature 531, 489-492 (2016).

The convention of classification of graphene nanoribbons as "zig-zag" and "armchair" is shown in Figure 2. The ribbon direction is y. The ribbon width is given by T.
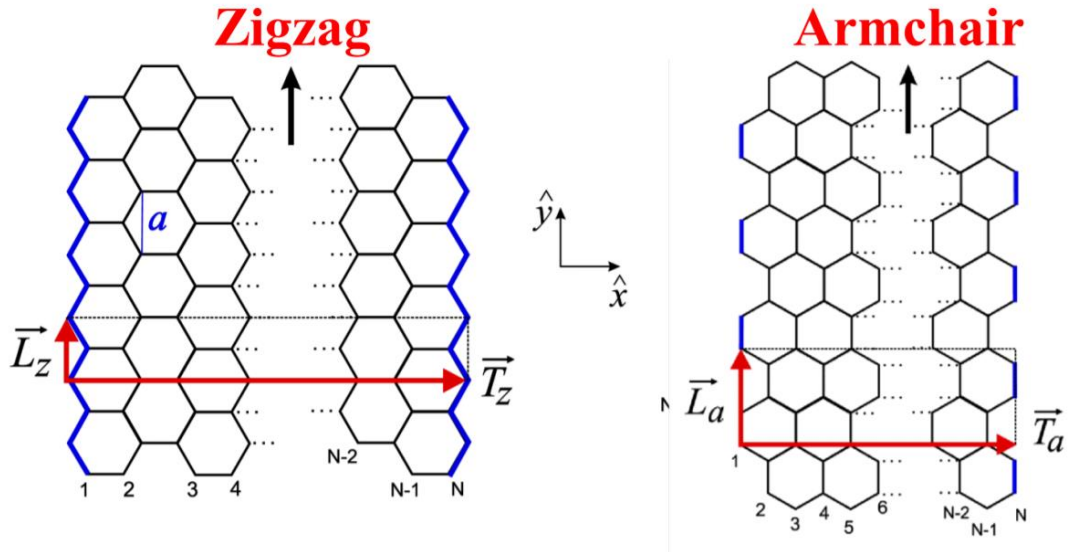
Figure 2: Naming convention for zig-zag and armchair ribbons, Illustration: Mildred Dresselhaus, MIT, Cambridge, MA

We are interested in zig-zag graphene nanoribbons because of the presence of edge states at the Fermi level. Such states are only present in the zig-zag configuration[2]. Spin-polarized calculations using the density functional theory (DFT) showed a gap opening, and the zig-zag edges become spin-polarized and antiferromagnetically ordered[3]. Also, previous studies proposed that application of an in-plane electric field perpendicular to the graphene nanoribbon could lead to a half-metal[4], where only one spin carries electric current. One can make use of such properties in several technological applications such as ribbon-based spintronics, sensors, and storage devices.

1.1   Theoretical perspective

The zig-zag graphene nanoribbons are one-dimensional strongly correlated systems[5,17]. The strong correlations in low-dimensional systems are due to the confinement of the particles in small phase space. This quantum confinement leads to strong inter-particle interaction, which results in quantum effects. To give an accurate physical description and interpretation of their properties in such systems, we need to consider correlation in the wavefunction. In order to do so, we need a high level of theory. The Density functional theory (DFT) and quantum Monte Carlo

(QMC) are two such methods that are capable of incorporating correlation effects to give an accurate description of a system. There are two categories of systems under consideration in case of zig-zag graphene nanoribbons,

1) Molecules with finite length, e.g., acenes.

2) Extended systems which are infinite, e.g., graphene nanoribbons. The periodic boundary conditions must be applied to such systems.

Several reports[6-8] on the molecular and extended zig-zag graphene nanoribbons have already been published claiming/verifying the proposal of Son[3] *et al.* that at the DFT-LDA level of theory the anti-ferromagnetic solution is the ground state.

Various attempts to include strong correlations in the system has been made by using Hubbard Hamiltonians[59,60]. However, our approach is to include correlations starting from the first principles in the QMC framework, which is a high-level theory more accurate than DFT.

A previous QMC report[9] suggests that in case of the narrowest width (single-ring width) molecular zig-zag graphene nanoribbons (acenes), the paramagnetic solution is the ground state.

1.2   Experimental Realization

Zig-zag graphene nanoribbon is a hot topic of interest due to its variety of technological applications, in particular for their potential use as in spintronic devices. Unfortunately, zig-zag graphene nanoribbons are very difficult to synthesize because of the instability due to its extremely reactive edges.
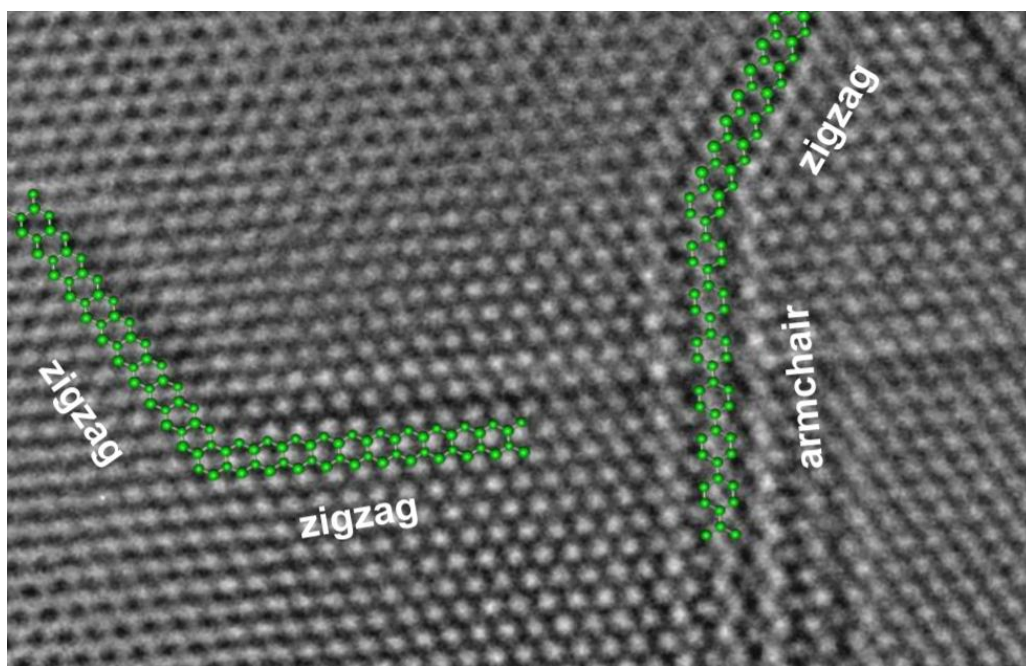
Figure 3: Atomic resolution image, taken from Campos-Delgado et al., Nano Letters (2008)

To date, there is only one example of the synthesis of zig-zag graphene nanoribbons. Group of Yang[10] *et al.* synthesized the zig-zag graphene nanoribbon through controlled chemical cascades[11] and properly chosen molecular precursors[10].

Our goal is to shed light on the correct description of the ground state of the zig-zag nanoribbons. To do so, we will use QMC as high-level method providing benchmark results, and compare its outcome with the most widely used DFT. At the end of this project, we would we able to explain/comment on the role of electron correlation in stabilizing the ground state of zig-zag graphene nanoribbons.

Chapter 2: Methods

For the calculation purpose, we had used two methods: Density functional theory (DFT) and quantum Monte Carlo (QMC). We will talk about each of these methods in detail, starting with the DFT.

2.1. Density functional theory

2.1.1. Introduction

The Density functional theory (DFT) is an *ab initio* technique used to calculate the electronic structure of many-body systems. It replaces the conventional *ab initio* wavefunction, which depends on 3N variables, by the electron density, which depends only on the three variables and hence reduces the complexity of the Schrödinger equation. The DFT method is mainly based on the two theorems given by Hohenberg and Kohn[12]. These theorems state that

1) The external potential is a unique functional of electron density.
2) The ground state can be obtained by minimizing the energy, which is a functional of electron density, with respect to electron density, and the electron density corresponding to the ground state energy is the ground-state electron density.

Solving the Schrödinger equation for interacting electrons is a mighty task or, we could say, a nearly impossible task as the equation becomes very complicated with high dimensionality:

$$\widehat{H}\Psi_i(r) = E\Psi_i(r). \tag{2.1}$$

Hence, with the use of above two theorems combined with the Born-Oppenheimer approximation,[55] the difficult problem of interacting electrons in a static external potential has been solved by mapping it to a relatively easy and solvable problem of non-interacting electrons in an effective potential while keeping the electron density same throughout the mapping. In simple words, it is a mapping of a many-particle Schrödinger equation to one-particle Schrödinger equation while keeping the electron density same:

$$\left[-\frac{1}{2}\nabla^2 + V_{Eff}(r)\right]\Psi_i(r) = \epsilon_i\Psi_i(r), \tag{2.2}$$

Here, V_{Eff} is the effective potential:

$$V_{Eff}(r) = V_{ext}(r) + V_H(r) + V_{XC}(r). \tag{2.3}$$

The Schrödinger equation is solved in a self-consistent manner[13]. The effective potential includes the external potential $V_{ext}(r)$, Hartree potential terms $V_H(r)$, and also takes care of the exchange and correlation interactions of electrons by different kinds of approximations/functionals. The exchange-correlation[14] part $V_{XC}(r)$ contains the difference between the kinetic energies of the interacting and non-interacting systems and also the electronic-correlation. Since the energy contribution from the exchange-correlation part is small compared to the total energy, so this term can be approximated. Please note that in case of strongly correlated systems, the exchange-correlation term is important and hence cannot be approximated, so we need high-level theories like QMC[15], DMRG[16], etc.

The simplest of these approximations or exchange-correlation functional is local-density approximation, also known as LDA[18,19]. The LDA is a class of functionals which are dependent only on the electron density at a point where the function is being evaluated. It assumes that exchange energy per particle at each point in space is the same as the exchange energy per particle in the uniform electron gas with the density equivalent to the density at this same point in space.

To cope with the problem of non-homogeneity of electron density, more advanced and accurate functionals are developed, which falls in the category of Generalized Gradient Approximation[20,21] (GGA). In GGA, the functionals depend on the electron density at a point and first derivative/gradient of electron density at that point as well.

Among the GGA functionals, I had used PBE[22] exchange-correlation functional. The PBE is an exchange-correlation functional which is applicable/suitable for a wide range of systems.

There is another set of exchange-correlation functionals known as hybrid functionals. In such functionals, a part exchange energy is replaced by exact exchange energy calculated from the Hartree-Fock Theory. The Hartree-Fock

method[23] is used to determine the wavefunction and energy of a many-body system. It uses the slater determinant approach for the approximation of many-body wavefunction. The Hartree-Fock method is also known as the self-consistent field (SCF) method as it assumes as if each particle is interacting with the mean-field created by all other particles, and the Schrödinger equation is solved in a self-consistent manner. The obtained Hartree-Fock energy is the exact exchange energy. I have had used a functional of this kind, which is known as GauPBE[24], the abbreviation of GaussianPBE. In GauPBE, short-range Hartree-Fock exchange is included in the functional using a Gaussian attenuation scheme. In this scheme, a gaussian term is incorporated in the Hartree-Fock exchange term, which gives more accurate results in solid-state bandgap calculations due to self-interaction error correction and is significantly faster than other functionals due to more rapid decay of the gaussian term.

2.1.2. Pseudo-potentials

We have used pseudo-potentials to optimize the wavefunction such that we can get significantly accurate results with the least computational cost.

We know that core electrons do not take part in the chemical bonding are strongly bound, which results in the screening of the nucleus and making the nucleus partially inert. Thus, the properties of metals and semiconductors are solely due to the loose valence electrons.

So, we can exploit this fact, and core electrons can be replaced by an ionic core, which is a good approximation of the potential felt by valence electrons from the core electrons. To fulfil the Pauli exclusion principle, orthogonality condition, the valence shell orbitals are oscillating near the core region. To represent these kinds of oscillating functions, we need a large number of plane waves, which is computationally expensive. To smoothen out the oscillations, we use a pseudo wavefunction that mimics the core region within a cut-off radius r_c and mimics the valence region outside.
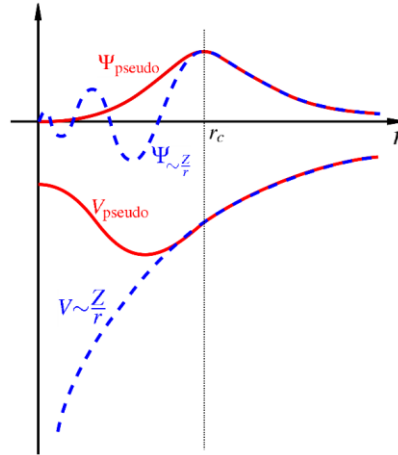
Figure 4: Comparison of a wavefunction in the Coulomb potential of the nucleus (blue) to the one in the pseudopotential (red). The real and the pseudo wavefunction and potentials match above a particular cut-off radius r_c. Illustration by Wolfram Quester.

2.1.3. Computational Details

All the DFT calculations were performed using the plane-wave[25] based QuantumESPRESSO[26,27] software. The PBE based GGA exchange and correlation functional have been used for the DFT calculations, and Ultra-soft Pseudopotential is considered for electron-ion interaction. The kinetic energy cut-off[28] and charge density cut-off used are 50 Ry and 200 Ry, respectively. The Brillouin zone is sampled with 24 k-points (24 X 1 X 1 Monkhorst-Pack grid[29]) in the ribbon direction and Marzari-Vanderbilt smearing[30] of 0.009 Ry is used for all the calculations. The vacuum separation between two periodic images, to avoid interaction, in Y and Z directions is 7.2 Å and 7 Å, respectively. In the second part, we used the GauPBE hybrid exchange-correlation functional. 6 q-points were used in the Brillouin zone. The Wannier[31] interpolation method was used in plotting the band structure to check the character of different orbitals in bands.

2.1.4. Limitations of DFT

DFT method is principle is exact but does not match experimental results as the fundamental quantity, the electron density, is obtained from the approximations done on the exchange-correlation part. Also, it is a well-established fact that the DFT does not give convincing results in case strongly correlated systems where strong correlations become significant.

2.2. Quantum Monte Carlo

2.2.1. Introduction

Quantum Monte Carlo (QMC)[15] is an *ab initio* method used to study complex and strongly correlated systems. Also, the QMC term refers to many different methods like Variational Monte Carlo, Diffusion Monte Carlo, Path Integral Molecular Dynamics, etc. In this project, we will use Variational Monte Carlo and Diffusion Monte Carlo.

Since DFT is unable to cope with strongly correlated systems, we used the QMC method. The advantage of QMC over DFT is that the former can explicitly consider the electron-electron correlation. At the variational Monte Carlo level, this is implemented by using a Jastrow term in the many-body QMC wavefunction. At the diffusion Monte Carlo level, correlation is included through a stochastic projection of the wave function towards the ground state.

Also, the precision of the calculation is directly related to the sample size. Therefore, we would easily tune[32] the precision of the results, according to the size of the MC sampling. The accuracy of the calculation also depends on the choice of the initial trial wavefunction. So, our efforts will be focused on improving this wavefunction, by optimizing its variational energy to be as close as possible to one of the ground states.

The first QMC step is the construction of the QMC correlated wavefunction,[52] $\Psi(r)$, which consists of the product of a determinant term and a Jastrow factor. The determinant part, $\Delta(r)$, encodes the fermionic anti-symmetry, while the Jastrow part, $J(r)$, is symmetric and spin-independent:

$$\Psi(r) = e^{-J(r)} . \Delta(\mathrm{r}). \tag{2.4}$$

The determinant part could take care of static correlations at different levels, while the Jastrow part takes care of the dynamic correlations (fraction of the correlation energy from spatial charge motion in the system).

In our study, the determinant part is represented by the anti-symmetrized geminal power (AGP)[33-36] which is determinant of a pairwise "geminal" function expanded in the Gaussian basis set:

$$\Delta(r) = \det\left[\phi(r, r')\right] = \sum_i \lambda_i \, \bar{\varphi}_i(r) \bar{\varphi}_i(r'). \tag{2.5}$$

The level of static correlation provided by the determinant part can be chosen based on the number of terms (virtual pair excitations) in the geminal expansion (above equation).

If the molecular orbitals expansion in the geminal is restricted up to N/2, then the wavefunction is a Jastrow single determinant (JSD):

$$\phi^{SD}(r,r') = \sum_{i=1}^{N/2} \lambda_i \, \bar{\varphi}_i(r)\bar{\varphi}_i(r'). \tag{2.6}$$

Here, φ are the molecular orbitals (MOs), N is the total number of electrons and λ_i are the coefficients in the geminal expansion.

If the geminal is expanded over a larger expansion (up to the full basis set), then it is called fully resonant Jastrow antisymmetric geminal power (JAGP):

$$\phi^{AGP}(r,r') = \sum_{ij} \lambda_{i,j} \, \chi_i(r)\chi_j(r'). \tag{2.7}$$

Here, χ are the atomic orbitals (AOs) and λ_{ij} are the parameters need to be optimized.

As mentioned before, the Jastrow part includes dynamic correlation. It consists of two parts, a homogenous (2-body Jastrow, J2) and an inhomogeneous part.

The inhomogeneous Jastrow is represented by a Gaussian basis set, which can contain on-site as well as inter-ion contributions:

$$J_1 = \sum_{lm} \alpha_{lm} \, G_l(r)G_m(r'). \tag{2.8}$$

Here, G's are the Gaussians centred at ions specified by l and m, while r and r' are electron coordinates. In our case, l and m refer to the same centre at the time, building up a three-body (electron-electron-ion) correlator. Here, α_{lm} are the parameters optimized during the QMC optimization.

On the other hand, the 2-body Jastrow is made of a radial form (depending only on the electron-electron distance):

$$J_2(r_1, \ldots, r_n) = \sum_{1 \le i \le j \le n} u(|r_i - r_j|), \tag{2.9}$$

where *u* is the radial function:

$$u(r) = \frac{1}{2\gamma}(1 - e^{-\gamma r}). \tag{2.10}$$

which fulfils cusp[37,38] conditions for particles with different spins. It removes the short-range divergence of the Coulomb interaction in the energy evaluation, by compensating this contribution by an equal and opposite divergence coming from the kinetic term due to the fulfilment of the above cusp conditions. Hence, it also results in a better convergence rate of the wavefunction energy optimization and in a stable diffusion Monte Carlo algorithm.

Since the QMC calculations are computationally very expensive, we optimize the QMC correlated wavefunction starting from an initial guess provided by performing a DFT calculation over the full primitive basis.

At variance with DFT, in QMC, we are using Gaussian basis sets[39] instead of plane waves, to reduce at most the size of the basis itself. Indeed, Gaussians converge usually faster than the plane waves, so they turn out to be computationally cheap.

To further reduce the basis set size, we contract it by finding the best set of hybrid-orbitals[40] required to achieve the desired accuracy at a low computational cost. To find the best hybrid orbitals, we maximize the overlap between the full basis wavefunction obtained by DFT and the one written in terms of contracted orbitals.

Once we find the best contraction, we could perform a DFT calculation on the converged k-mesh using a contracted basis. Then we look for the Baldereschi point,[41] a special point in the Brillouin zone, where the DFT energy is equal (or numerically very close) to the DFT energy on the converged k-mesh. The use of the Baldereschi point is meant to reduce the finite-size errors, coming from the finite simulation cell, mimicking the infinite system.

Upon fixing the contracted basis set and generating the DFT orbitals at the Baldereschi point, we add the Jastrow factor to the DFT determinant, and we optimize the wave function at the QMC level. In the first optimization step, we optimize the Jastrow linear coefficients and freeze the determinant part. Then, we also optimize the exponents of the Gaussian basis of the Jastrow part.

After these steps, we optimize the parameters in the determinant and the Jastrow part simultaneously. At the end of all these optimizations, the trial wavefunction is ready for the Variational Monte Carlo (VMC) step.[42]

The variational principle guarantees that energy optimization gives us the best upper bound to the true ground state energy (E_0):

$$E_v \approx \frac{\int \Psi_T^*(R)\widehat{H}\Psi_T(R)\,dR}{\int \Psi_T^*(R)\Psi_T(R)\,dR} \geq E_0.$$ (2.11)

The Metropolis algorithm[43] is used to sample a set, R_m, of electronic configurations drawn from the configuration-space probability density given by $\Psi^2(R)$ normalized. A single trajectory made of these points is called "walker." The local energy is then evaluated at each of these points by the Metropolis and averaged over the whole set to give the variational energy:

$$E_v \approx \frac{1}{M}\sum_{m=1}^{M} E_L(R_m),$$ (2.12)

Here, $E_L(R_m)$ is the local energy, defined as:

$$E_L(r) = \frac{\widehat{H}\Psi_T(r)}{\Psi_T(r)}.$$ (2.13)

The last step of the QMC method is the Lattice Regularized Diffusion Monte Carlo (LRDMC).[44] The LRDMC is a lattice regularized version of the standard diffusion Monte Carlo (DMC) algorithm. Like DMC, the LRDMC is a stochastic projection method to solve the imaginary-time Schrödinger equation:

$$-\partial_t \Phi(R,t) = (\widehat{H} - E_T)\Phi(R,t).$$ (2.14)

In case of Fermions, we get a sign problem in the projection scheme, since translational probabilities will not be positive definite, due to the Fermionic anti-symmetry of the wave function. To tackle the sign problem, we use the fixed-node approximation (FNA),[45-47] which implies that sign-flipping moves will be disregarded in such a way that a walker will evolve only within a given nodal pocket. The wave function nodes are determined by the optimization performed at the QMC level. The LRDMC method projects the VMC energy towards the true ground state energy within the FNA.

The above calculations are performed for supercells of increasing size, in order to approach the thermodynamic limit, which is estimated through a finite-size (FS) extrapolation. Simulation of extended systems using periodic boundary conditions introduces many-body finite-size (FS) error.[54]

In QMC calculations, there are three ways of reducing the FS error.

1) By performing unit cell and supercell calculations at a special point (Baldereschi point) in the Brillouin zone.
2) By applying two-body corrections using the KZK[53] energy functional.
3) By explicitly extrapolating the results, obtained for different supercell sizes, to the thermodynamic limit.

2.2.2. Computational details

All the calculations, both DFT and QMC, are performed using the TurboRVB package,[48] which is based on the Jastrow correlated geminal power wave function. The QMC wave functions are represented in the Gaussian basis sets. The triple zeta basis set, (cc-pVTZ),[49,50] is used in the calculations, optimized for the carbon atom pseudopotential (Filippi).[51] The hydrogen is taken without pseudization, and its basis set is of triple zeta correlation consistent type (cc-pVTZ). This basis has been contracted to reduce the computational cost, and speed up the calculations with sufficient accuracy. The contracted basis for our calculations consists of 9 C and 2 H atomic orbitals. For the DFT calculations, the LDA exchange-correlation functional is used. The KZK corrections were obtained by performing DFT calculations using the KZK energy functional.

Chapter 3: Results and Discussion

In this chapter, we are going to provide the data we obtained by performing calculations, and parallelly we will analyze and discuss the results obtained.

3.1. DFT

We had performed the DFT calculations with the PBE and GauPBE exchange-correlation (XC) functionals. The systems under consideration were ribbons with width 2 (the smallest one) up to 6 (the largest one we considered in DFT). We performed calculations for paramagnetic (NM), ferromagnetic (FM), and anti-ferromagnetic (AFM) configurations. Both functionals give the AFM configuration as the ground state for all the ribbons. Also, localized edge states were found at the Fermi level.

We also calculated the band structure in all cases, as shown in Figs. 5 and 6 for PBE and GauPBE, respectively. In both cases, it could be seen that the bandgap closes as a function of the ribbon width. One more important thing we observed is that the band gaps are always indirect, although it is difficult to observe it from Fig. 5 because the k-shifts of the gaps are about 10^{-2} in crystal units, thus too small for the scale of the plot. The most remarkable difference between GauPBE and PBE is the fact that the bandgaps are larger in GauPBE as compared to PBE, as reported in Tab. 2.

Table 1: Energies per C atom for zig-zag ribbons as a function of ribbon width. The calculations are done at the PBE and the GauPBE level of theories.

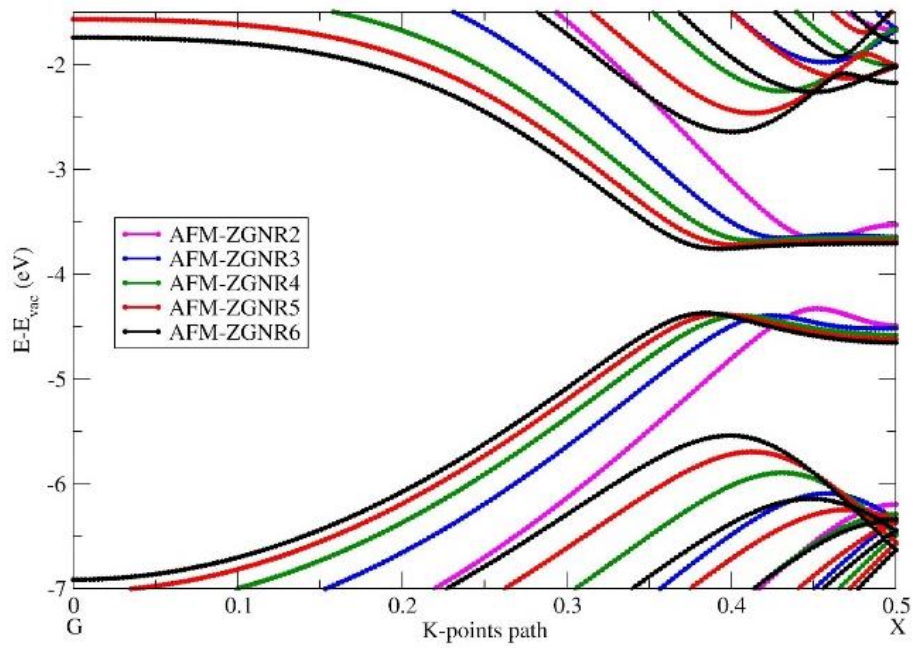| Width of the Ribbon	AFM (Ha)		FM (Ha)		NM (Ha)	
	PBE	GauPBE	PBE	GauPBE	PBE	GauPBE
2	-5.98650	-5.99880	-5.98630	-5.99796	-5.98630	-5.99769
3	-5.88982	-5.90044	-5.88967	-5.89986	-5.88954	-5.89919
4	-5.84167	-5.85205	-5.84160	-5.85175	-5.84138	-5.85123
5	-5.81283	-5.82278	-5.81279	NA	-5.81259	-5.82215
6	-5.79362	-5.80329	-5.79358	NA	-5.79341	-5.80270

Band Sturucture of ZGNR with different widths

Figure 5: Band structure for zig-zag ribbons with different widths at the PBE level.

Band structure of ZGNR's of different width
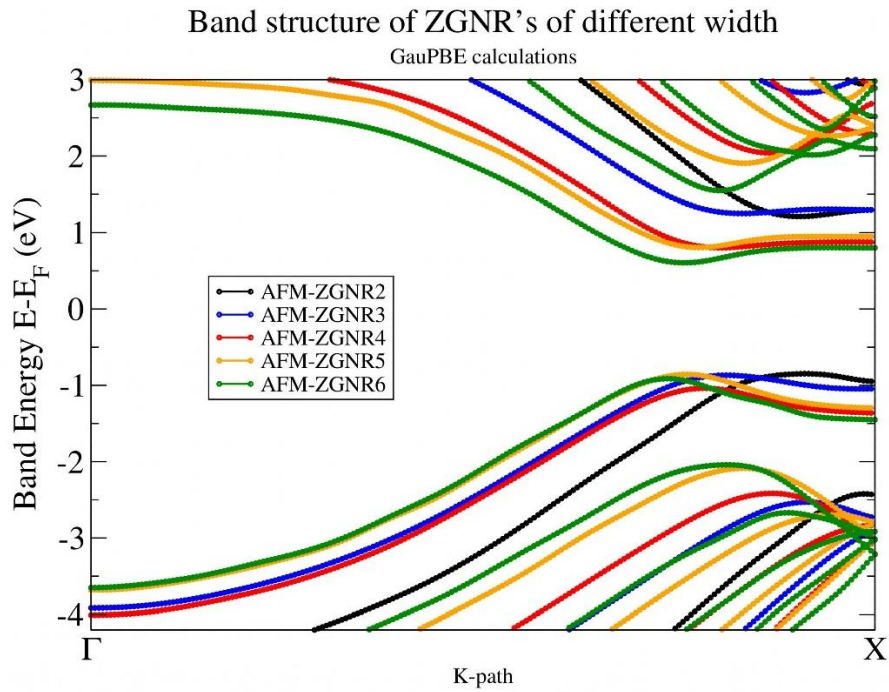
GauPBE calculations

Figure 6: Band structure for zig-zag ribbons with different widths at the Gau-PBE level.

24

Table 2: Bandgaps as a function of ribbon width. All the bandgaps reported here are indirect.

Configuration and width/XC-Functional	AFM-ZGNR2	AFM-ZGNR3	AFM-ZGNR4	AFM-ZGNR5	AFM-ZGNR6
PBE	0.66	0.74	0.713	0.66	0.613
GauPBE	2.06	2.12	1.84	1.66	1.52

The energy gains of AFM and FM phases are computed in Tab. 3 with respect to the paramagnetic case, taken as reference. We plot these values in Fig. 7. One can observe that at both PBE and GauPBE levels, the energy difference between AFM and FM configuration vanishes as a function of the zig-zag ribbon width because the spin coupling between the edges gets smaller and smaller as the ribbon width increases. At the GauPBE level, the AFM configuration is a lot more stable than the one at the PBE level. We will use these gains while comparing these results with the ones obtained by QMC.

Table 3: Gain in energies per carbon atom as a function of zig-zag ribbon width. The ferromagnetic configuration melts down to the paramagnetic one in PBE for the narrowest ribbon.

Width of the Ribbon	AFM-NM (meV)		FM-NM (meV)	
	PBE	GauPBE	PBE	GauPBE
2	-5.5	-30.2	0[*]	-7.3
3	-7.4	-34.1	-3.6	-18.3
4	-7.8	-22.3	-6.0	-14.2
5	-6.6	-17.1	-5.4	NA
6	-5.9	-16.0	-4.8	NA

By looking at the lattice parameters evolution for the systems analyzed here, there are no significant changes across different widths. As far as the magnetic properties are concerned in the magnetic phases, the local magnetic moment of the edge atom is nearly constant as a function of the ribbon width. Instead, the total absolute magnetization per unit cell increases, as reported in Tab. 4, because of the additional contribution from the inner carbon atoms.

Table 4: Total absolute magnetization in antiferromagnetic conf as a function of ribbon width.

System →	AFM (width 2)	AFM (width 3)	AFM (width 4)	AFM (width 5)	AFM (width 6)
Total absolute magnetization $(\frac{\mu_B}{a_0{}^2})$	0.55	0.79	0.89	0.98	1.04

The results obtained by us are somewhat similar to what Son and co-workers had found. The most relevant difference is the bandgaps values, much smaller than the ones we obtained. We believe that the reason for this is the use of a different exchange-correlation functional. Son and co-workers had done their calculations at the local spin density approximation (LSDA) level of theory, while our calculations are based on the GGA approximation.
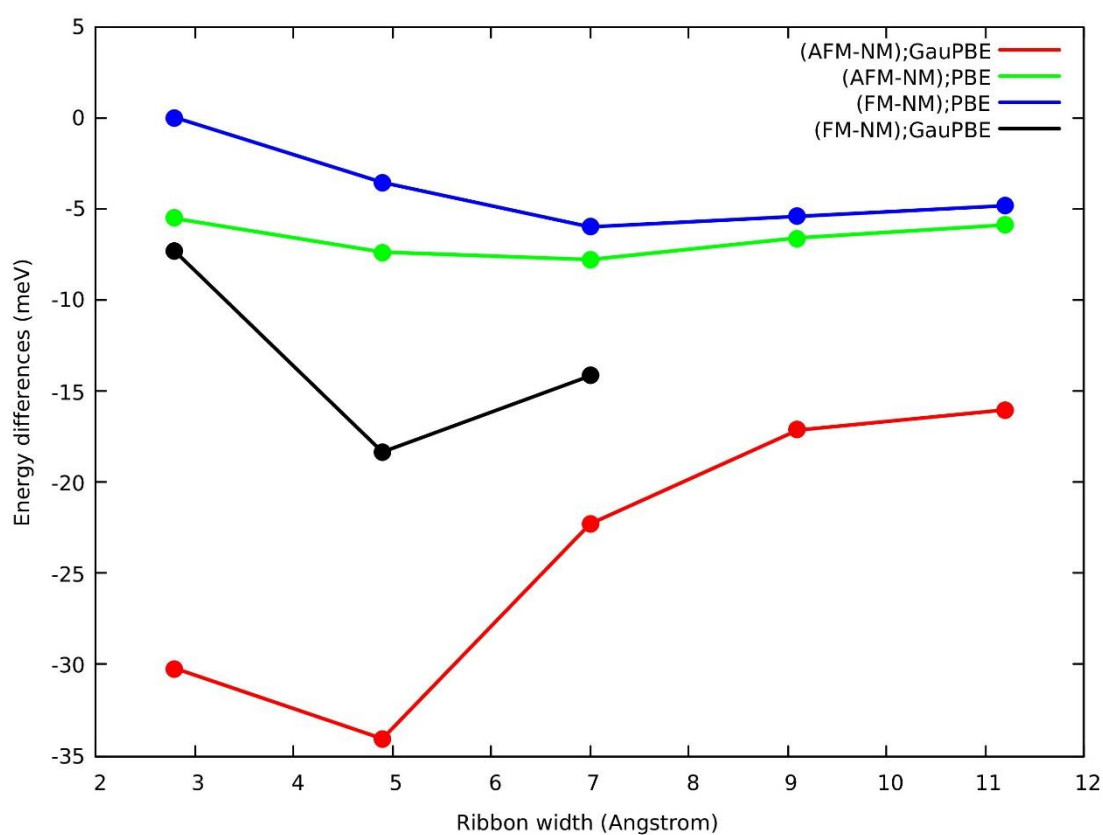

Figure 7: Energy gain per C atom as a function of ribbon width (width in Angstrom).

(a)

(b)

(c)
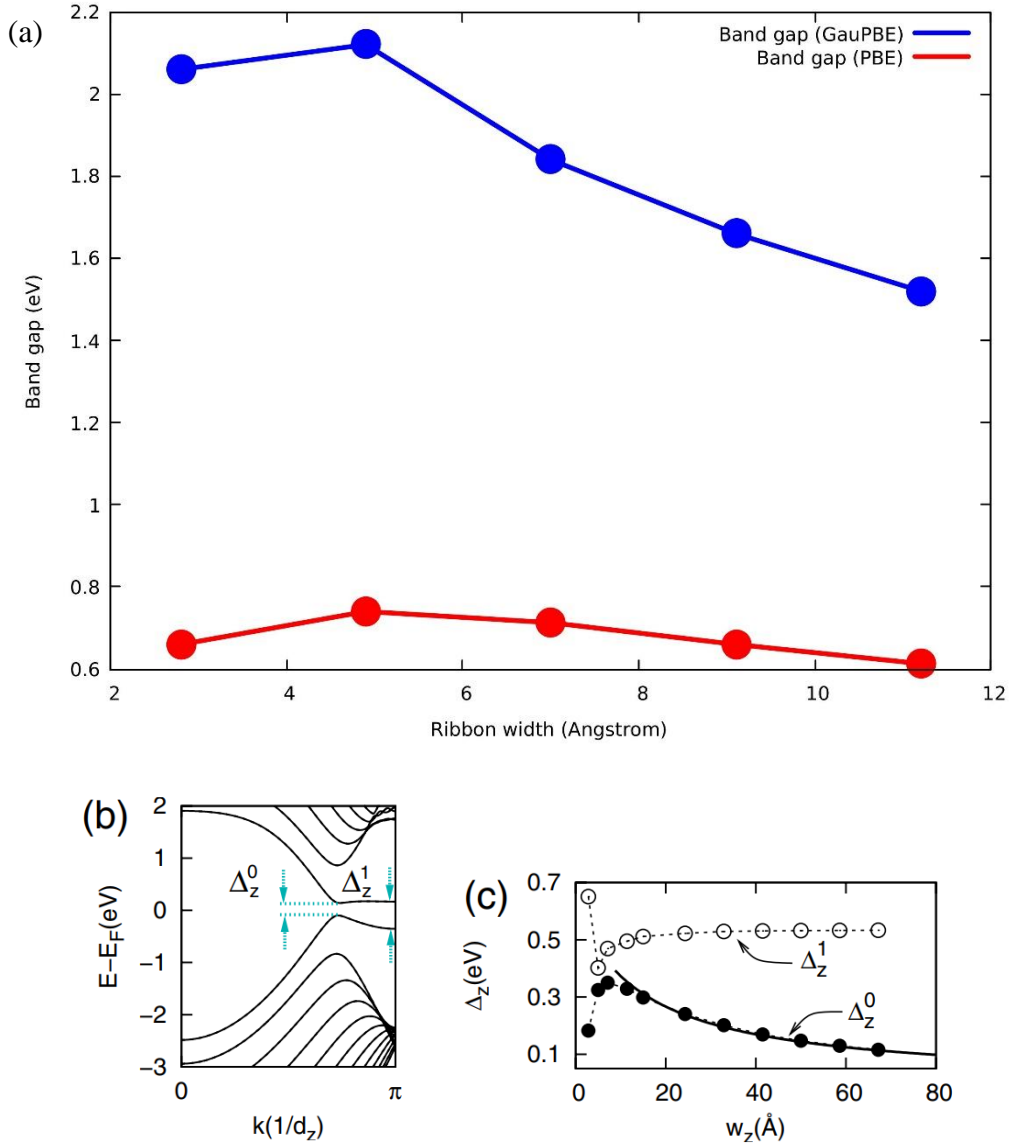
Figure 8: (a) Bandgap as a function of ribbon width with PBE (violet) and GauPBE(green) XC-functionals (b) Band structure of zig-zag graphene nanoribbon calculated by Son et al. at LSDA level of theory. (c) Bandgap as a function of ribbon width calculated at LSDA level of theory, reported by Son et al.

From the Wannierization of the *ab initio* Hamiltonian, we then studied the orbital character of the bands. By looking at the band structure projected onto three different sets of orbitals, i.e., $C(p_z)$, $C(sp^2)$, and $H(s)$, plotted in Figs. 9, 10, and 11, respectively, it appears that the orbitals close to the Fermi level have a strong p_z character, while the $H(s)$ are mainly located in the conduction bands.

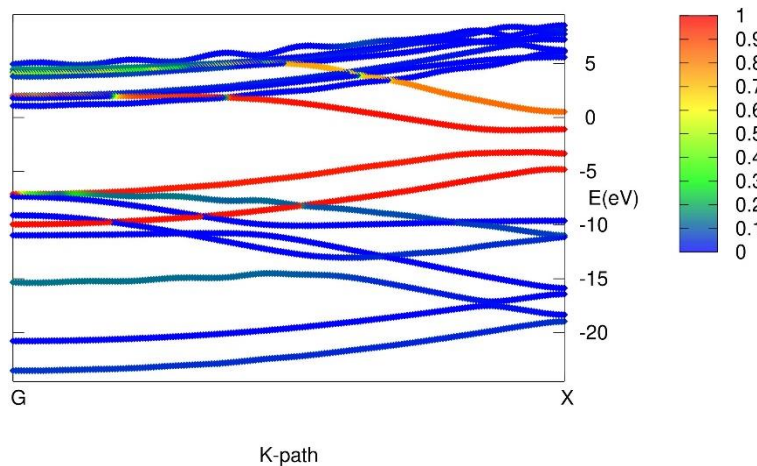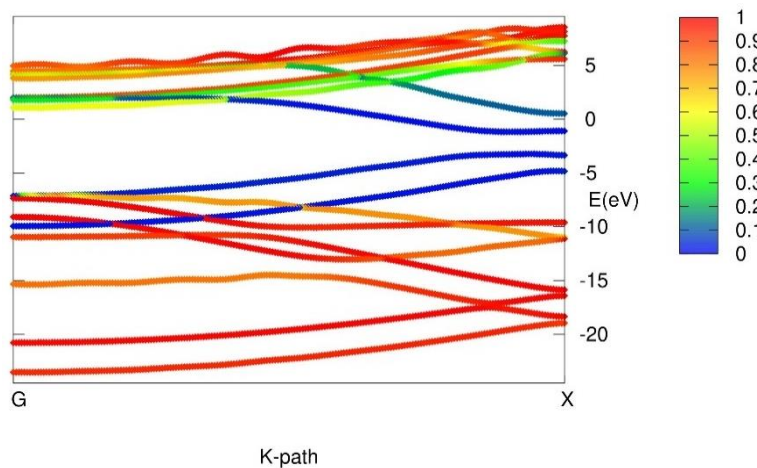*Figure 9: C(p_z) orbital contribution to the band structure*
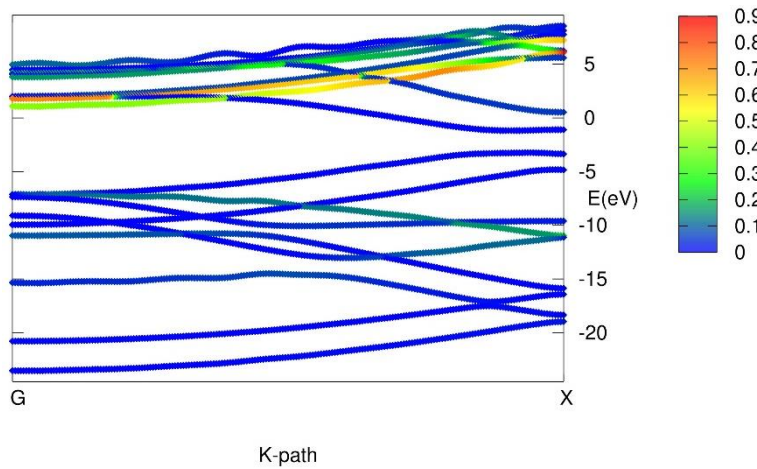

Figure 10: C(sp^2) orbital contribution.

Figure 11: H (s) orbital contribution

After finishing calculations for the unit cell, we also carried out supercell PBE calculations to check whether the spin order breaks the underlying lattice translational symmetry, as we go to longer ribbons. We used two rings long ribbon and varied the width up to 3 rings. We observed that local spins along the carbon edges are ferromagnetically coupled, while the coupling across the edges is anti-ferromagnetic. These couplings do not change as a function of length or width of the ribbon. So, we could say that as we change the size of ribbon in both directions, the nature of the ground state does not change, always staying in an AFM configuration.

We could see that the results obtained using the DFT method varies widely, and depend strongly on the type of exchange-correlation functional used. The bandgaps and the energetics of various phases predicted with three functionals (LSDA, PBE, and GauPBE) are very different, and we are not in a position to comment on which functional is giving the most accurate results. Since zig-zag graphene nanoribbons are strongly correlated systems, and the XC-functionals bear approximations which fail for strong electronic correlation, we need a higher level of theory to treat electron correlation more precisely. In this respect, QMC is the method of choice. Indeed, it is well established that QMC gives a more reliable description of strongly correlated systems, as it can explicitly consider the electron-electron correlation by using a Jastrow term in the many-body QMC wavefunction, or by projecting the many-body wave function towards the true ground state of the system within FNA.

3.2. QMC

Given the technical difficulty of performing many-body QMC calculations from first principles, and their high computational cost, we could study the narrowest ribbon (ZGNR2) only, during the period of this internship. The ZGNR2 system has been studied, using four types of variational wave functions in the QMC framework:

1. Jastrow correlated single determinant wave function (corresponding to the paramagnetic case);
2. Jastrow correlated AGP wave function (corresponding to a correlated paramagnet, eventually superconducting in the infinite size limit);
3. Spin-polarized wave function (corresponding to the ferromagnetic phase);
4. Spin-broken wave function with antiferromagnetic order.

For all these wave functions, we followed the same procedure, which we illustrate as follows. We started by taking the ribbon geometry optimized at the PBE level in the NM state. We obtained the determinant part of the QMC wavefunction by performing a DFT calculation using the Gaussian primitive cc-pVTZ basis set. Then we performed basis set contractions, reported in Tab. 5, to get the desired accuracy at a less computational expense.

Table 5: Optimization of the basis set using hybrid orbitals

Basis set	Energy per C atom (Ha)	Overlap with primitive cc-pVTZ
Primitive cc-pVTZ	-5.95858	1.00000
4C&2H	-5.75062	0.89992
7C&2H	-5.95597	0.99927
9C&2H	-5.95802	0.99983
12C&2H	-5.95802	0.99984

We started by choosing four contracted (or hybrid) orbitals for the carbon atom (4C) and 2 contracted (hybrid) orbitals for hydrogen (2H) and determined the optimal contraction coefficients by maximizing the overlap of the contracted basis set wave function with the one expanded in the primitive cc-pVTZ basis set. By looking at the weights of the contracted orbitals and at the DFT energies in the contracted basis set, a minimum of 2H hybrid orbitals is enough to be within 0.5 mH from the cc-pVTZ energy. Still, the dependence of the DFT energy on the atomic orbital contractions for

the carbon atom is significantly stronger, as shown in Tab. 5. So, we tuned the number of contracted carbon orbitals till convergence within the 0.5 mH threshold. From Tab. 5, we concluded that 9C and 2H Gaussian hybrid orbitals are the optimal basis set to fulfil the required accuracy.

We used the contracted basis set to find the Baldereschi point and then performed a DFT calculation on this point. The wavefunction obtained by doing a DFT on the Baldereschi point is used as the starting point for the subsequent QMC calculations.

To correlate the Slater determinant generated by DFT, we applied a Jastrow factor leading to the QMC wave function in Eq. 2.4. In order to find the best trial wave function in the variational sense (i.e. as close as possible to the ground state), we optimize the variational parameters by minimizing the QMC energy of the variational wave function. The linear and exponential coefficients of the Jastrow part (Eq. 2.8-10) are optimized in the first QMC step. In the second step, the linear and exponentials coefficients of the Determinant and Jastrow parts are optimized simultaneously. In Figs.12 and 13, we can see the parameters evolution and the energy convergence during the latest QMC optimization step.

In Fig. 12, we can follow the evolution of the α_{ij} parameters, in the three-body Jastrow term (Eq. 2.8), over the number of iterations in the QMC energy minimization.

Similarly, we could follow the evolution of other parameters like γ in the two-body Jastrow and λ_{ij} in the determinant part of the QMC wavefunction.

Also, in Figure 13, we can track the trajectory of the total energy of a system during the QMC energy minimization. We plotted the energies of Jastrow correlated AGP wave functions obtained with different orbital expansions, during their optimization history.
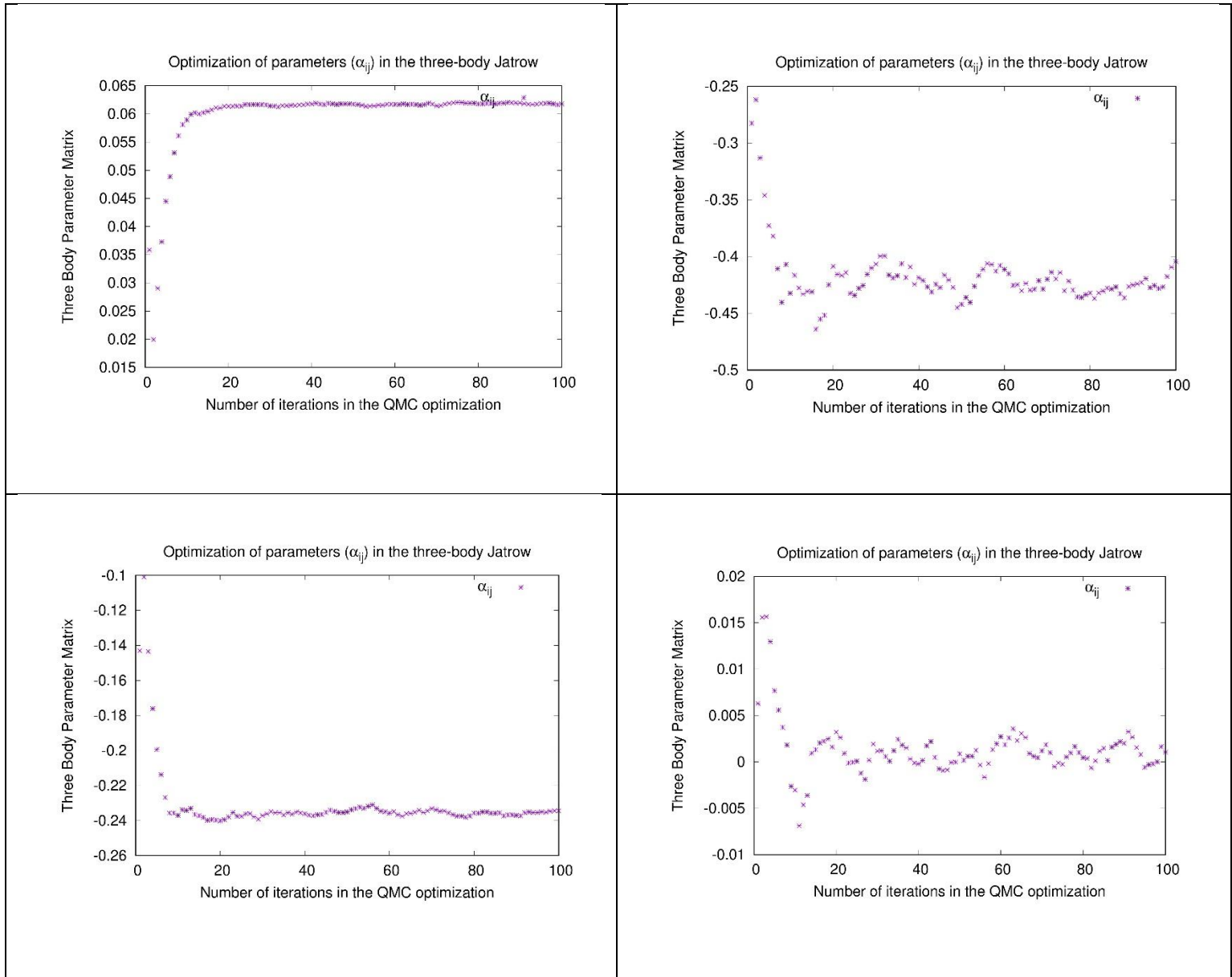
Figure 12: Convergence of three-body Jastrow parameters during the QMC optimization.
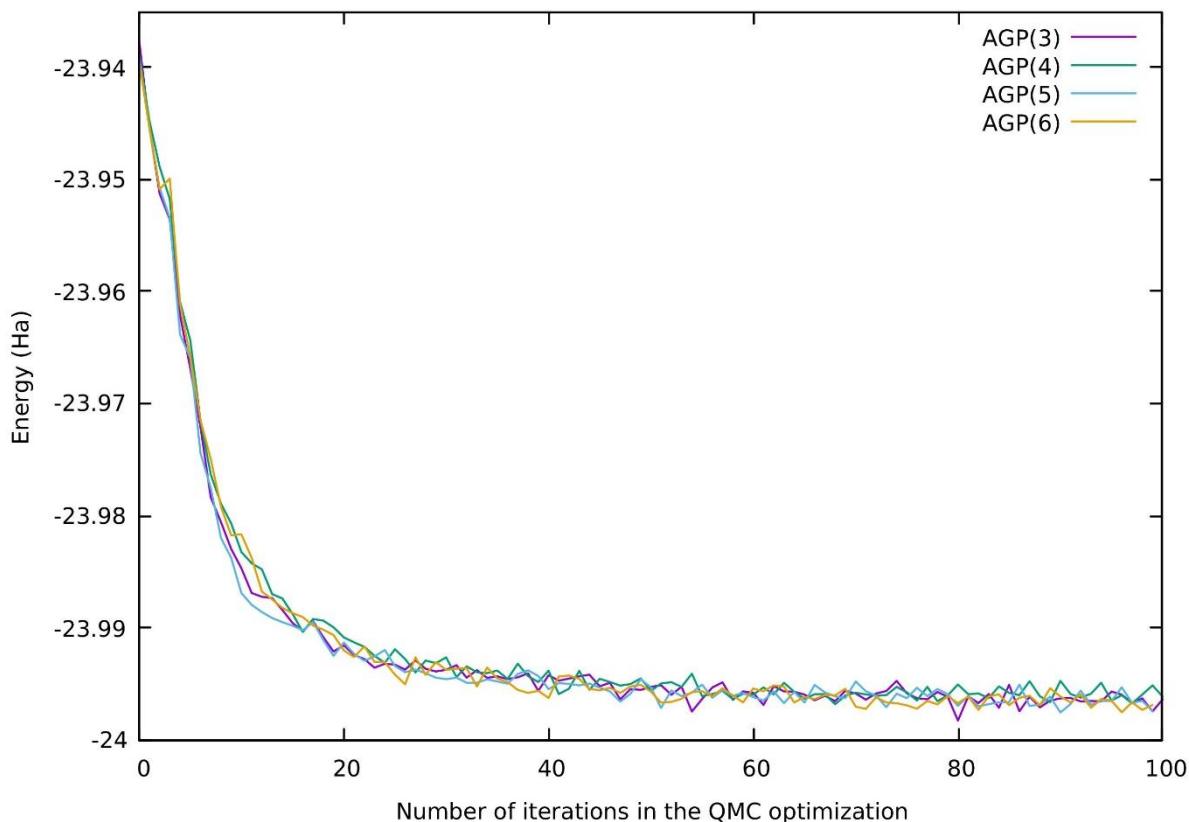
Figure 13: Convergence of energy during the QMC optimization for different orbital expansions in the AGP. AGP(N), N: number of MOs above HOMO in the AGP expansion.

Once the wavefunction is fully optimized, we performed the VMC calculation using the optimized trial wavefunction. After obtaining the VMC energy, we projected the wavefunction towards the ground state using LRDMC within FNA.

We performed the QMC calculations for four supercell sizes, one-, three-, six-, and nine-ring supercells, for finite-size extrapolation.

We repeated the same procedure for all wave functions taken into account in our study.

1) JSD paramagnetic wave function

In Tab. 6 and Fig.14, we show the energetics of the paramagnetic phase as a function of the supercell size.

Table 6: Energies for the paramagnetic case at the VMC and LRDMC level

Number of Carbon atoms (N)	E_{VMC}/N (Ha)	σ_{VMC}/N (Ha)	E_{LRDMC}/N (Ha)	σ_{LRDMC}/N (Ha)
4	-5.99587	0.00004	-6.00617	0.00029
12	-5.97900	0.00003	-5.99077	0.00005
36	-5.97312	0.00001	-5.98568	0.00004
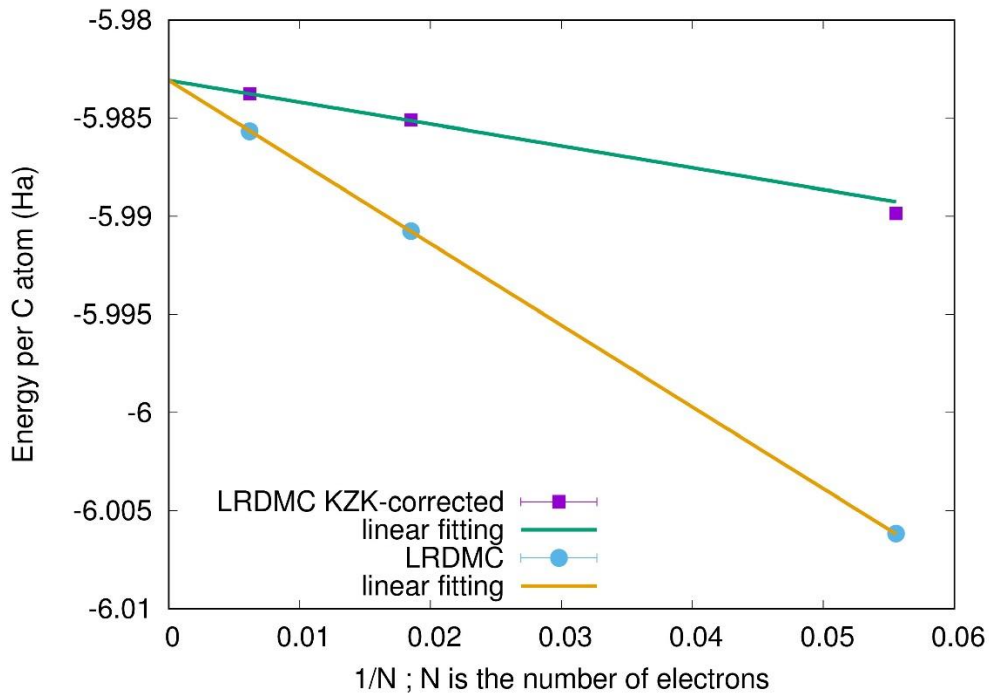
Figure 14: FS Extrapolation of the LRDMC results for the paramagnetic case.

2) JAGP wave function

We also studied the variational energy of the JAGP wave function, which included correlations beyond JSD. In particular, the JAGP will introduce correlations in the antisymmetric part of the wave function of singlet type, typical of a superconductor in the resonating valence bond theory. We expand the AGP in terms of molecular orbitals above HOMO (Eq. 2.7), which correspond to virtual electron pair excitations, and we study the effect of this expansion in the VMC and LRDMC energies. We learned that the excitations increase the variational freedom and hence stabilizes the system. After

three MOs beyond HOMO, which is 1/3rd of the MOs in the SD, the energy was converged. We kept this ratio the same for a larger number of rings as well, to perform the finite size extrapolation.

Similarly, we computed the energy gain (Tab. 7) in AGP, with respect to the SD, as a function of the number of virtual excitations in the AGP.

Table 7: The VMC, LRDMC energies, and gain in energies obtained for SD and AGP with the different number of virtual pair excitations in the AGP expansion.

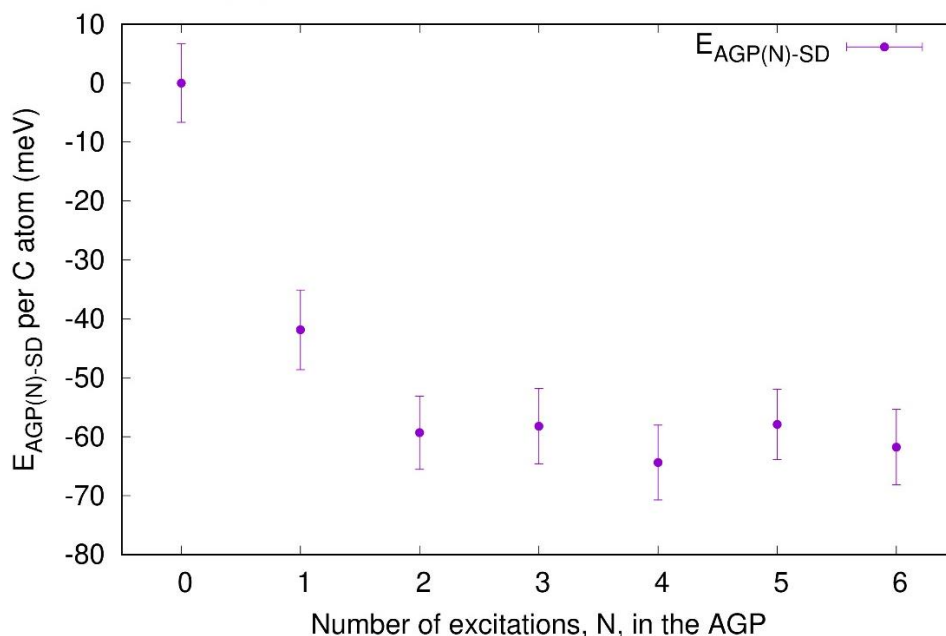| Number of excitations in the AGP (N)	E_{VMC}/N (Ha)	σ_{VMC}/N (Ha)	E_{LRDMC}/N (Ha)	σ_{LRDMC}/N (Ha)	$E_{(AGP-SD)}/N$ (meV)	$\sigma_{(AGP-SD)}/N$ (meV)
0/SD	-5.99602	0.00003	-6.00621	0.00017	0.0	6.7
1	-5.99842	0.00003	-6.00775	0.00018	-41.9	6.8
2	-5.99911	0.00003	-6.00839	0.00015	-59.3	6.2
3	-5.99910	0.00003	-6.00835	0.00016	-58.2	6.4
4	-5.99910	0.00003	-6.00858	0.00016	-64.4	6.4
5	-5.99920	0.00003	-6.00834	0.00013	-57.9	6.0
6	-5.99923	0.00004	-6.00848	0.00016	-61.8	6.4

Figure 15: LRDMC energy gain as a function of the number (N) of MOs above HOMO (virtual pair excitations) in the AGP expansion.
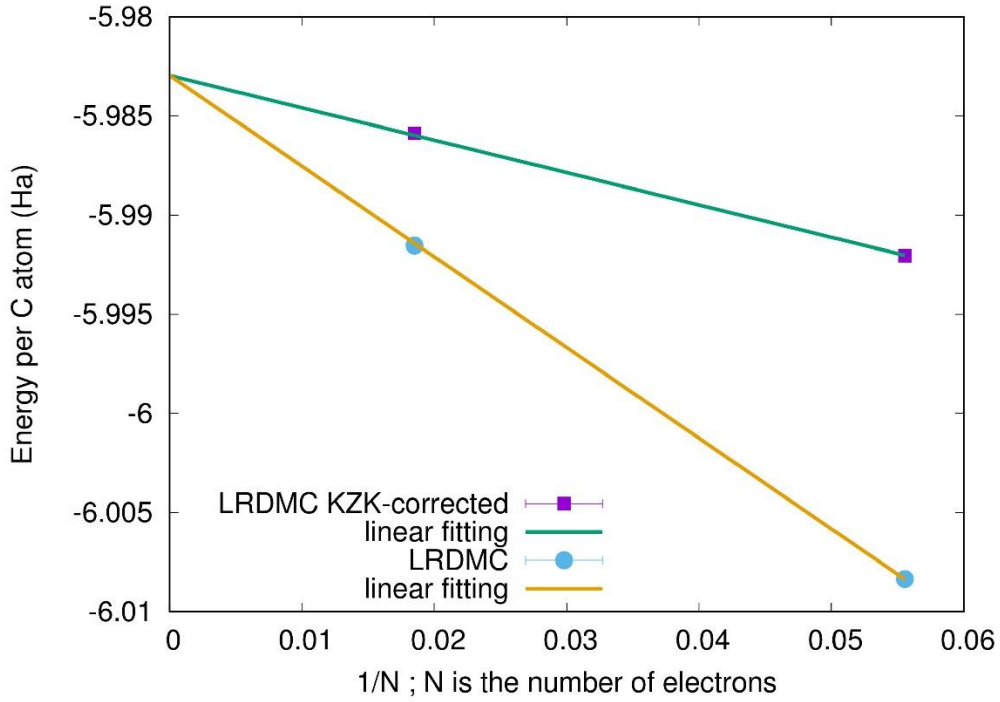
Figure 16: FS Extrapolation of the LRDMC results for the AGP.

3) Spin-polarized ferromagnetic wave function

We generated the ferromagnetic configuration by fixing the magnetic moment of 2 BM per unit cell (two unpaired electrons). We used the contracted basis set and the Baldereschi point which we had used for the paramagnetic case so that the results between the two states will be in a one-to-one correspondence. After going throughout the optimization procedure, we obtained the energies per carbon shown in Tab. 8.

Table 8: Energies per carbon atom for the ferromagnetic case at the VMC and LRDMC level.

Number of carbon atoms (N)	E_{VMC}/N (Ha)	σ_{VMC}/N (Ha)	E_{LRDMC}/N (Ha)	σ_{LRDMC}/N (Ha)
4	-5.95761	0.00009	-5.97585	0.00017
12	-5.94121	0.00006	-5.95701	0.00013
24	-5.93702	0.00005	-5.95457	0.00018
36	-5.93557	0.00005	-5.95214	0.00021
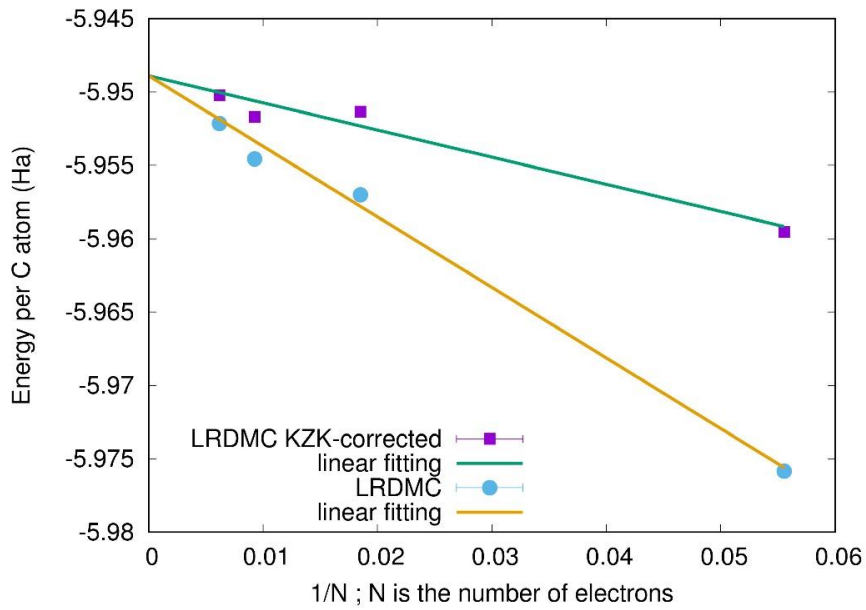
Figure 17: FS Extrapolation of the LRDMC results for the ferromagnetic wave function.

In Fig. 18, the surface magnetization is plotted for the ferromagnetic wavefunction for 3-ring supercell. It can be seen that the nature and quantity of local magnetic moment on the opposite edges are the same, which is characteristic of the FM phase.
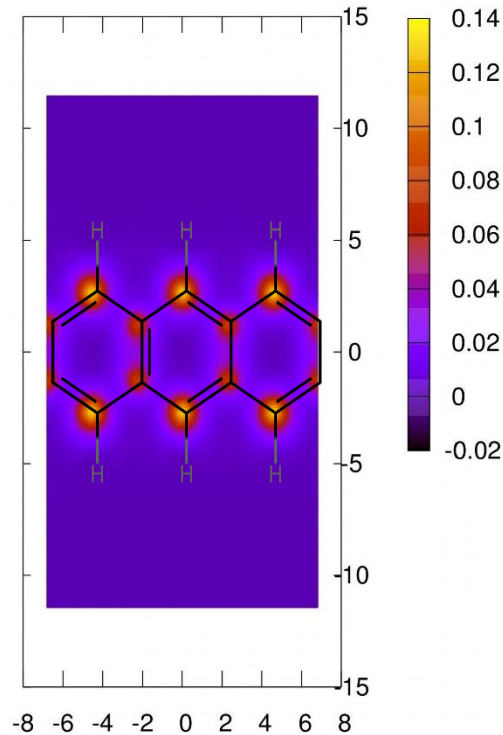
Figure 18: Contour plot of surface magnetization $(\frac{\mu_B}{a_0{}^2})$ for the ferromagnetic case.

4) Spin-broken antiferromagnetic wave function

Similarly, we generated the antiferromagnetic configurations by fixing the magnetic moment to zero BM per unit cell. We used the same contracted basis set and Baldereschi points which we used in the paramagnetic case. We optimized the wavefunction and performed VMC and LRDMC calculations and extrapolated the results to the thermodynamic limit.

In case of a single unit cell, the AFM phase melts upon optimizing the determinant part in the QMC optimization. The reason for this meeting could be the loose local interactions in the unit cell which becomes stronger in supercells.

Table 9: Energies per carbon atom for the antiferromagnetic case at the VMC and LRDMC level.

| Number of carbon atoms (N)	E_{VMC}/N (Ha)	σ_{VMC}/N (Ha)	E_{LRDMC}/N (Ha)	σ_{LRDMC}/N (Ha)
12	-5.98251	0.00001	-5.99196	0.00005
24	-5.97904	0.00001	-5.98852	0.00003
36	-5.97752	0.00001	-5.98717	0.00005
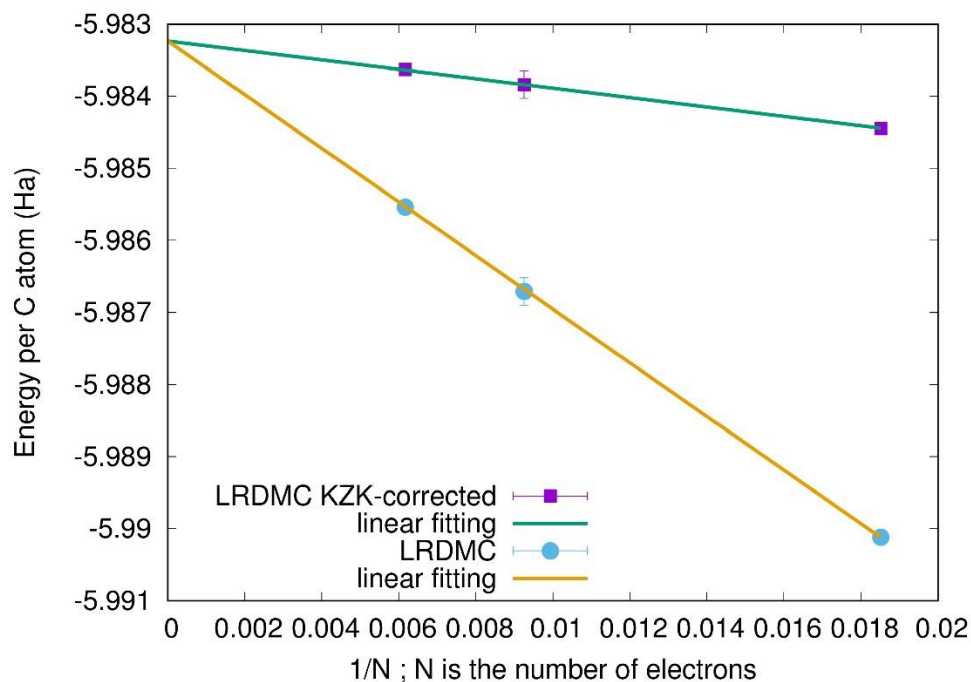
Figure 19: FS Extrapolation of the LRDMC results for the antiferromagnetic wave function.

38

In Fig. 20, the surface magnetization is plotted for the antiferromagnetic wave function for 3-ring supercell. It can be seen that the nature and quantity of local magnetic moment on the opposite edges is opposite and equal, which is characteristic of the AFM phase. Also, the ferromagnetic coupling is happening along the edges.

Figure 20: Contour plot of the surface magnetization $(\frac{\mu_B}{a_0{}^2})$ for the antiferromagnetic wave function.

Chapter 4: Conclusions

All the conclusions we made in this thesis are valid for the narrowest width zig-zag graphene nanoribbon only.

Table 10: Energy differences per C atom at a different level of theories.

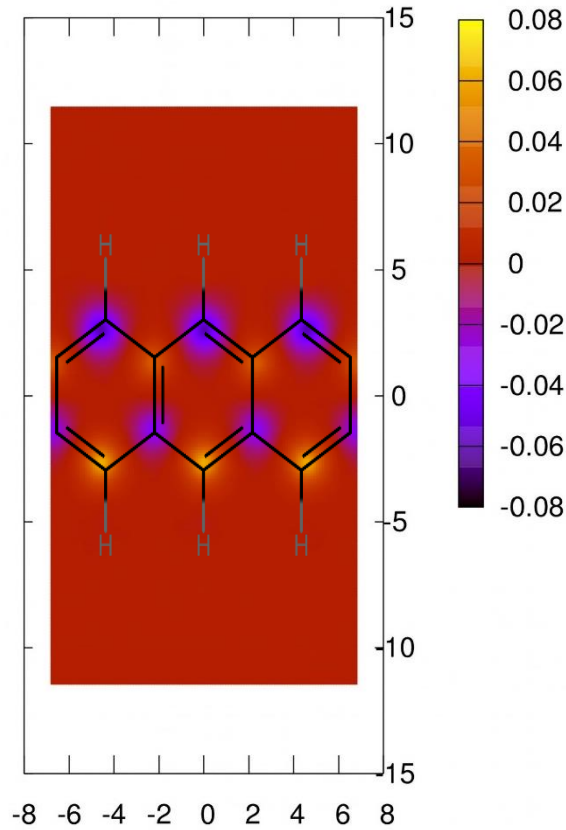| Level of theory used (only for the narrowest width)	FM-NM (meV)	AFM-NM (meV)	JAGP-JSD (meV)
DFT PBE	0.0	-5.5	-
DFT GauPBE	-7.3	-30.2	-
LRDMC (3-ring supercell)	918.5 ± 3.8	-9.4 ± 1.9	-22.3 ± 6.0
LRDMC (9-ring supercell)	911.5 ± 5.8	-37.4 ± 1.7	NA
LRDMC (Thermodynamic limit)	930.4 ± 15.6	-49.5 ± 3.2	3.3 ± 5.0

1) From Tab. 10, the QMC calculations validate the Gau-PBE results, by predicting the static AFM state as lower in energy than the paramagnetic phase for the narrowest zig-zag graphene nanoribbon in the extrapolated thermodynamic (infinite length) limit.

2) In the thermodynamic limit, the gain in energy from the singlet pairing in the AGP expansion goes to zero. However, the error bar in these calculations is still too large to discard the possibility that more correlated paramagnetic wave functions (i.e. beyond the JSD ansatz) would be the actual ground state of the system. Other calculations are necessary to clarify this point.

3) For the energetics of such strongly correlated systems, the GauPBE XC-functional performs much better than the PBE XC-functional, as it gives results closer to the QMC method for the energy gain between AFM and PM phase. Accordingly, the magnetic moments (see Tab.11) predicted by the Gau-PBE XC functional are also in better agreement with QMC than the ones obtained by the PBE XC functional. So, if we take QMC as a reference, PBE seems to underestimate the magnetization, while GauPBE slightly overestimates it.

4) *Table 11: Total absolute magnetization, for the narrowest AFM ribbon as a function of supercell.*

System →	AFM (unit cell)	AFM (3 units)	AFM (6 units)	AFM (9 units)
Absolute magnetization ($\frac{\mu B}{a_0{}^2}$)	-	0.469±0.0008	0.800±0.0005	0.919±0.0007

5) For the narrowest width, FM phase melts at the PBE level, and it is certainly not the GS at the GauPBE level, being always bound from below by the AFM phase. From Tab. 10, the QMC energies of the FM phase are much larger than the ones obtained by DFT, because we studied only the QMC wave function at fixed spin polarization with $S_z=2$ (i.e. the smallest polarization accessible by QMC in the unit cell). Calculations at fractional spin polarization are ongoing for the largest supercell (9 rings), to check whether there is a stability window for this phase.

Perspectives

These results open interesting perspectives. The most immediate step forward will be the completion of the analysis of more correlated wave functions (beyond JSD), which could challenge the AFM phase as the ground state. JAGP is one of them (we need to reduce the error bars for the calculations with this wave function). Also, Jastrow correlated Pfaffian wave functions could be studied by allowing the AF magnetic moments to fluctuate. Indeed, in quasi-one-dimensional systems magnetic fluctuations are believed to be dominant. In strictly one-dimensional systems the Lieb's theorem[58] states that these magnetic fluctuations are so strong that they destroy any magnetic order. From this viewpoint, this theorem cannot be applied directly to our system because even for the narrowest ribbon the transverse direction is not negligible. Therefore, further calculations are necessary to include magnetic fluctuations beyond the static magnetic patterns.

An important point to be addressed is the coupling between the electronic states and the geometry of the ribbon. The relevant point here is to study the structural instabilities[56,57] due to cis and trans conformations in the ribbon.

Finally, an interesting follow-up would be the study of the evolution of the phase diagram as a function of ribbon width, as we have done at the DFT level, for both PBE and Gau-PBE.

References

(1) Lee, C.; Wei, X.; Kysar, J. W.; Hone, J. Measurement of the Elastic Properties and Intrinsic Strength of Monolayer Graphene. Science 2008, 321 (5887), 385–388. https://doi.org/10.1126/science.1157996.

(2) Nakada, K.; Fujita, M.; Dresselhaus, G.; Dresselhaus, M. S. Edge State in Graphene Ribbons: Nanometer Size Effect and Edge Shape Dependence. Physical Review B 1996, 54 (24), 17954–17961. https://doi.org/10.1103/physrevb.54.17954.

(3) Son, Y.-W.; Cohen, M. L.; Louie, S. G. Energy Gaps in Graphene Nanoribbons. Physical Review Letters 2006, 97 (21). https://doi.org/10.1103/physrevlett.97.216803.

(4) Son, Y.-W.; Cohen, M. L.; Louie, S. G. Half-Metallic Graphene Nanoribbons. Nature 2006, 444 (7117), 347–349. https://doi.org/10.1038/nature05180.

(5) Kirova, N.; Brazovskii, S. Conjugated Polymers at the Verge of Strongly Correlated Systems and 1D Semiconductors. Synthetic Metals 2004, 141 (1), 139–147. https://doi.org/10.1016/j.synthmet.2003.09.024.

(6) Wu, C.-S.; Chai, J.-D. Electronic Properties of Zigzag Graphene Nanoribbons Studied by TAO-DFT. Journal of Chemical Theory and Computation 2015, 11 (5), 2003–2011. https://doi.org/10.1021/ct500999m.

(7) Correa, J. H.; Pezo, A.; Figueira, M. S. Braiding of Edge States in Narrow Zigzag Graphene Nanoribbons: Effects of Third-Neighbor Hopping on Transport and Magnetic Properties. Physical Review B 2018, 98 (4). https://doi.org/10.1103/physrevb.98.045419.

(8) Jiang, D.; Sumpter, B. G.; Dai, S. Unique Chemical Reactivity of a Graphene Nanoribbon's Zigzag Edge. The Journal of Chemical Physics 2007, 126 (13), 134701. https://doi.org/10.1063/1.2715558.

(9) Dupuy, N.; Casula, M. Fate of the Open-Shell Singlet Ground State in the Experimentally Accessible Acenes: A Quantum Monte Carlo Study. The Journal of Chemical Physics 2018, 148 (13), 134112. https://doi.org/10.1063/1.5016494.

(10) Ruffieux, P.; Wang, S.; Yang, B.; Sánchez-Sánchez, C.; Liu, J.; Dienel, T.; Talirz, L.; Shinde, P.; Pignedoli, C. A.; Passerone, D.; et al. On-Surface Synthesis of

Graphene Nanoribbons with Zigzag Edge Topology. Nature 2016, 531 (7595), 489–492. https://doi.org/10.1038/nature17151.

(11) Dorel, R.; Echavarren, A. M. Strategies for the Synthesis of Higher Acenes. European Journal of Organic Chemistry 2016, 2017 (1), 14–24. https://doi.org/10.1002/ejoc.201601129.

(12) Hohenberg, P.; Kohn, W. Inhomogeneous Electron Gas. Physical Review 1964, 136 (3B), B864–B871. https://doi.org/10.1103/physrev.136.b864.

(13) Kohn, W.; Sham, L. J. Self-Consistent Equations Including Exchange and Correlation Effects. Physical Review 1965, 140 (4A), A1133–A1138. https://doi.org/10.1103/physrev.140.a1133.

(14) Kaxiras, E. Atomic and Electronic Structure of Solids https://www.cambridge.org/core/books/atomic-and-electronic-structure-of-solids/1B7E5043BE2B6D12C749AB9A1E913295 (accessed Mar 23, 2020).

(15) Foulkes, W. M. C.; Mitas, L.; Needs, R. J.; Rajagopal, G. Quantum Monte Carlo Simulations of Solids. Reviews of Modern Physics 2001, 73 (1), 33–83. https://doi.org/10.1103/revmodphys.73.33.

(16) Schollwoeck, U. The Density-Matrix Renormalization Group. Reviews of Modern Physics 2005, 77 (1), 259–315. https://doi.org/10.1103/RevModPhys.77.259.

(17) Ronning, F.; Batista, C. Strongly Correlated Electron Systems. Journal of Physics: Condensed Matter 2011, 23 (9), 090201. https://doi.org/10.1088/0953-8984/23/9/090201.

(18) Ceperley, D. M.; Alder, B. J. Ground State of the Electron Gas by a Stochastic Method. Physical Review Letters 1980, 45 (7), 566–569. https://doi.org/10.1103/physrevlett.45.566.

(19) Perdew, J. P.; Zunger, A. Self-Interaction Correction to Density-Functional Approximations for Many-Electron Systems. Physical Review B 1981, 23 (10), 5048–5079. https://doi.org/10.1103/physrevb.23.5048.

(20) Perdew, J. P.; Chevary, J. A.; Vosko, S. H.; Jackson, K. A.; Pederson, M. R.; Singh, D. J.; Fiolhais, C. Atoms, Molecules, Solids, and Surfaces: Applications of the

Generalized Gradient Approximation for Exchange and Correlation. Physical Review B 1992, 46 (11), 6671–6687. https://doi.org/10.1103/physrevb.46.6671.

(21) Perdew, J. P.; Wang, Y. Accurate and Simple Analytic Representation of the Electron-Gas Correlation Energy. Physical Review B 1992, 45 (23), 13244–13249. https://doi.org/10.1103/physrevb.45.13244.

(22) Perdew, J. P.; Burke, K.; Ernzerhof, M. Generalized Gradient Approximation Made Simple. Physical Review Letters 1996, 77 (18), 3865–3868. https://doi.org/10.1103/physrevlett.77.3865.

(23) Fischer, C. F. Self-Consistent-Field (SCF) and Multiconfiguration (MC) Hartree-Fock (HF) Methods in Atomic Calculations: Numerical Integration Approaches. Computer Physics Reports 1986, 3 (5), 274–325. https://doi.org/10.1016/0167-7977(86)90001-8.

(24) Song, J.-W.; Yamashita, K.; Hirao, K. Communication: A New Hybrid Exchange Correlation Functional for Band-Gap Calculations Using a Short-Range Gaussian Attenuation (Gaussian-Perdue–Burke–Ernzerhof). The Journal of Chemical Physics 2011, 135 (7), 071103. https://doi.org/10.1063/1.3628522.

(25) Kresse, G.; Furthmüller, J. Efficiency of Ab-Initio Total Energy Calculations for Metals and Semiconductors Using a Plane-Wave Basis Set. Computational Materials Science 1996, 6 (1), 15–50. https://doi.org/10.1016/0927-0256(96)00008-0.

(26) Giannozzi, P.; Baroni, S.; Bonini, N.; Calandra, M.; Car, R.; Cavazzoni, C.; Ceresoli, D.; Chiarotti, G. L.; Cococcioni, M.; Dabo, I.; et al. QUANTUM ESPRESSO: A Modular and Open-Source Software Project for Quantum Simulations of Materials. Journal of Physics: Condensed Matter 2009, 21 (39), 395502. https://doi.org/10.1088/0953-8984/21/39/395502.

(27) Giannozzi, P.; Andreussi, O.; Brumme, T.; Bunau, O.; Buongiorno Nardelli, M.; Calandra, M.; Car, R.; Cavazzoni, C.; Ceresoli, D.; Cococcioni, M.; et al. Advanced Capabilities for Materials Modelling with Quantum ESPRESSO. Journal of Physics: Condensed Matter 2017, 29 (46), 465901. https://doi.org/10.1088/1361-648x/aa8f79.

(28) Alfè, D.; Gillan, M. J. Efficient Localized Basis Set for Quantum Monte Carlo Calculations on Condensed Matter. Physical Review B 2004, 70 (16). https://doi.org/10.1103/physrevb.70.161101.

(29) Monkhorst, H. J.; Pack, J. D. Special Points for Brillouin-Zone Integrations. Physical Review B 1976, 13 (12), 5188–5192. https://doi.org/10.1103/physrevb.13.5188.

(30) Marzari, N.; Vanderbilt, D.; Payne, M. C. Ensemble Density-Functional Theory for *Ab initio* Molecular Dynamics of Metals and Finite-Temperature Insulators. Physical Review Letters 1997, 79 (7), 1337–1340. https://doi.org/10.1103/physrevlett.79.1337.

(31) Mostofi, A. A.; Yates, J. R.; Lee, Y.-S.; Souza, I.; Vanderbilt, D.; Marzari, N. Wannier90: A Tool for Obtaining Maximally-Localized Wannier Functions. Computer Physics Communications 2008, 178 (9), 685–699. https://doi.org/10.1016/j.cpc.2007.11.016.

(32) Feller, W. An Introduction to Probability Theory and Its Applications. Volume I; Wiley, [Or 1: New York, 1970.

(33) A. C. Hurley, John Edward Lennard-Jones and John Anthony Pople 1997The molecular orbital theory of chemical valency XVI. A theory of paired-electrons in polyatomic molecules Proc. R. Soc. Lond. A220446–455. https://doi.org/10.1098/rspa.1953.0198.

(34) Bratož, S.; Durand, P. Transposition of the Theories Describing Superconducting Systems to Molecular Systems. Method of Biorbitals. The Journal of Chemical Physics 1965, 43 (8), 2670–2679. https://doi.org/10.1063/1.1697193.

(35) Bratož, S.; Durand, P. Transposition of the Theories Describing Superconducting Systems to Molecular Systems. Method of Biorbitals. The Journal of Chemical Physics 1965, 43 (8), 2670–2679. https://doi.org/10.1063/1.1697193.

(36) Bessis, G.; Murez, C.; Bratož, S. Méthode Des Biorbitales: Application Préliminaire Au Calcul de l'Energie de l'Etat Fondamental de l'Atome de Beryllium. International Journal of Quantum Chemistry 1967, 1 (4), 327–335. https://doi.org/10.1002/qua.560010404.

(37) Kato, T. On the Eigenfunctions of Many-Particle Systems in Quantum Mechanics. Communications on Pure and Applied Mathematics 1957, 10 (2), 151–177. https://doi.org/10.1002/cpa.3160100201.

(38) Pack, R. T.; Brown, W. B. Cusp Conditions for Molecular Wavefunctions. The Journal of Chemical Physics 1966, 45 (2), 556–559. https://doi.org/10.1063/1.1727605.

(39) Petruzielo, F. R.; Toulouse, J.; Umrigar, C. J. Compact and Flexible Basis Functions for Quantum Monte Carlo Calculations. The Journal of Chemical Physics 2010, 132 (9), 094109. https://doi.org/10.1063/1.3342062.

(40) Sorella, S.; Devaux, N.; Dagrada, M.; Mazzola, G.; Casula, M. Geminal Embedding Scheme for Optimal Atomic Basis Set Construction in Correlated Calculations. The Journal of Chemical Physics 2015, 143 (24), 244112. https://doi.org/10.1063/1.4938089.

(41) Baldereschi, A. Mean-Value Point in the Brillouin Zone. Physical Review B 1973, 7 (12), 5212–5215. https://doi.org/10.1103/physrevb.7.5212.

(42) Sorella, S. Wave Function Optimization in the Variational Monte Carlo Method. Physical Review B 2005, 71 (24). https://doi.org/10.1103/physrevb.71.241103.

(43) Metropolis, N.; Rosenbluth, A. W.; Rosenbluth, M. N.; Teller, A. H.; Teller, E. Equation of State Calculations by Fast Computing Machines. The Journal of Chemical Physics 1953, 21 (6), 1087–1092. https://doi.org/10.1063/1.1699114.

(44) Casula, M.; Filippi, C.; Sorella, S. Diffusion Monte Carlo Method with Lattice Regularization. Physical Review Letters 2005, 95 (10). https://doi.org/10.1103/physrevlett.95.100201.

(45) Anderson, J. B. A Random-walk Simulation of the Schrödinger Equation: H+3. The Journal of Chemical Physics 1975, 63 (4), 1499–1503. https://doi.org/10.1063/1.431514.

(46) Moskowitz, J. W.; Schmidt, K. E.; Lee, M. A.; Kalos, M. H. A New Look at Correlation Energy in Atomic and Molecular Systems. II. The Application of the Green's Function Monte Carlo Method to LiH. The Journal of Chemical Physics 1982, 77 (1), 349–355. https://doi.org/10.1063/1.443612.

(47) Reynolds, P. J.; Ceperley, D. M.; Alder, B. J.; Lester, W. A. Fixed-node Quantum Monte Carlo for Moleculesa) B). The Journal of Chemical Physics 1982, 77 (11), 5593–5603. https://doi.org/10.1063/1.443766.

(48) Nakano, K.; Attaccalite, C.; Barborini, M.; Capriotti, L.; Casula, M.; Coccia, E.; Dagrada, M.; Genovese, C.; Luo, Y.; Mazzola, G.; et al. TurboRVB: A Many-Body Toolkit for {*Ab initio*} Electronic Simulations by Quantum Monte Carlo. arXiv:2002.07401 [cond-mat, physics: physics] 2020.

(49) Kendall, R. A.; Dunning, T. H.; Harrison, R. J. Electron Affinities of the First-row Atoms Revisited. Systematic Basis Sets and Wave Functions. The Journal of Chemical Physics 1992, 96 (9), 6796–6806. https://doi.org/10.1063/1.462569.

(50) Davidson, E. R. Comment on "Comment on Dunning's Correlation-Consistent Basis Sets." Chemical Physics Letters 1996, 260 (3), 514–518. https://doi.org/10.1016/0009-2614(96)00917-7.

(51) Burkatzki, M.; Filippi, C.; Dolg, M. Energy-Consistent Pseudopotentials for Quantum Monte Carlo Calculations. The Journal of Chemical Physics 2007, 126 (23), 234105. https://doi.org/10.1063/1.2741534.

(52) Jastrow, R. Many-Body Problem with Strong Forces. Physical Review 1955, 98 (5), 1479–1484. https://doi.org/10.1103/physrev.98.1479.

(53) Kwee, H.; Zhang, S.; Krakauer, H. Finite-Size Correction in Many-Body Electronic Structure Calculations. Physical Review Letters 2008, 100 (12). https://doi.org/10.1103/physrevlett.100.126404.

(54) Kent, P. R. C.; Hood, R. Q.; Williamson, A. J.; Needs, R. J.; Foulkes, W. M. C.; Rajagopal, G. Finite Size Errors in Quantum Many-Body Simulations of Extended Systems. Physical Review B 1999, 59 (3), 1917–1929. https://doi.org/10.1103/PhysRevB.59.1917.

(55) Born, M.; Oppenheimer, R. Zur Quantentheorie Der Molekeln. Annalen der Physik 1927, 389 (20), 457–484. https://doi.org/10.1002/andp.19273892002.

(56) Kivelson, S.; Chapman, O. L. Polyacene and a New Class of Quasi-One-Dimensional Conductors. PhRvB 1983, 28 (12), 7236–7243. https://doi.org/10.1103/PhysRevB.28.7236.

(57) Dos Santos, M. C. Electronic Properties of Acenes: Oligomer to Polymer Structure. Physical Review B 2006, 74 (4). https://doi.org/10.1103/physrevb.74.045426.

(58) Dutta, S.; Wakabayashi, K. Magnetization Due to Localized States on Graphene Grain Boundary. Scientific Reports 2015, 5 (1). https://doi.org/10.1038/srep11744.

(59) Raghu, C.; Pati, Y. A.; Ramasesha, S. Structural and Electronic Instabilities in Polyacenes: Density-Matrix Renormalization Group Study of a Long-Range Interacting Model. Physical Review B 2002, 65 (15). https://doi.org/10.1103/physrevb.65.155204.

(60) Srinivasan, B.; Ramasesha, S. Structural Instability in Polyacene: A Projector Quantum Monte Carlo Study. Physical Review B 1998, 57 (15), 8927–8933. https://doi.org/10.1103/physrevb.57.8927.